Available online at www.sciencedirect.com
ScienceDirect
J. of Supercritical Fluids 42 (2007) 410–418
THE JOURNAL OF Supercritical Fluids
www.elsevier.com/locate/supflu

Growth of magnetic thin films using CO_2 RESS expansions

Silvia De Dea [a], Dominic Graziani [b], David R. Miller [a,*], Robert E. Continetti [b]

[a] *Department of Mechanical and Aerospace Engineering, University of California, San Diego, 9500 Gilman Drive, La Jolla, CA 92093-0001, USA*
[b] *Department of Chemistry and Biochemistry, University of California, San Diego, 9500 Gilman Drive, La Jolla, CA 92093-0340, USA*

Received 2 August 2006; received in revised form 1 November 2006; accepted 5 November 2006

Abstract

A continuous-flow rapid expansion of supercritical solution (RESS) apparatus is used to grow thin iron oxide thin films under ambient and vacuum conditions. The magnetic thin films are produced by expanding a supercritical solution of ferric acetylacetonate ($Fe(acac)_3$) and CO_2 and directing the resulting supersonic jet onto both hot and cold silicon wafers. The concentration of the expanding solution is monitored in-line with a UV–vis high pressure view cell which is also used to perform solubility measurements. The resulting films contain nano- and sub-micronic particles in the 13–700 nm size range and show magnetic order. Structural and magnetic data for these thin particle films have been obtained by SQUID and SEM measurements and compared as a function of substrate surface temperature, growth times, and initial solute concentrations. Experimental and theoretical analysis of the thermodynamics and fluid mechanics appropriate for this RESS process is discussed.

Keywords: Supercritical fluids; Nanoparticles; Iron oxide; Magnetic particles; Rapid expansion of supercritical solutions; Ferric acetylacetonate

1. Introduction

Metal organic compounds have received considerable interest as precursors for the formation of metal oxide thin films, sensors and magnetic nanoparticles [1]. In particular iron oxide magnetic particles have attracted interest due to their applications in recording media, ferrofluids, catalysts and targeted drug delivery [2]. New synthetic routes for the preparation of magnetic nanoparticles and thin films are under constant investigation and some of them include spray pyrolysis [3]. In this work we present the application of the RESS technique [4] to the formation of magnetic thin films using the metal organic compound ferric acetylacetonate ($Fe(acac)_3$) as a precursor. Since its earliest use to form films and powders [5], RESS has been applied widely to form particles and films of a variety of materials including ceramics [6], drugs [7], and polymers [8]. A recent overview of broader applications of supercritical fluids to nanomaterials, including RESS, is that by Reverchon and Adami [9]. In the process design and utilization of RESS it is important to acquire accurate solubility data and for a continuous process to monitor on-line the composition of the expanding solution. For this purpose we introduced a spectroscopic UV–vis cell in the RESS system, prior to the expansion.

Although RESS has been studied extensively, there has been little advancement in its application to magnetic nanoparticle formation. This is due to the very low solubility of transition metal oxides in supercritical fluids (SCFs). In fact, given the nonpolar nature of SC-CO_2, most of the solid ionic metal salts do not dissolve directly. Therefore, we chose $Fe(acac)_3$ as an iron oxide precursor since the acetylacetonate ligands, being nonpolar, increase the solubility of the metal ion in the supercritical fluid phase. An extensive review on the solubility of several chelating agents and metal containing compounds in SC-CO_2 was published by Poliakoff and co-worker [10].

We describe the RESS apparatus, our solubility data, and preliminary data on the $Fe(acac)_3/CO_2$ system and the characteristics of deposited thin films. In addition we discuss our approach to model the thermodynamics, kinetics, and fluid mechanics of the RESS process.

2. Experimental

Fig. 1 shows a schematic of the RESS apparatus which includes a CO_2 cylinder, a supercritical continuous pump (Thar Technology, P-50), a heating bath, a bypass line, an extraction vessel, and a UV–vis cell, followed by a RESS source expansion

* Corresponding author. Tel.: +1 8585343131; fax: +1 8585345355.
E-mail address: dmiller@ucsd.edu (D.R. Miller).

0896-8446/$ – see front matter © 2006 Elsevier B.V. All rights reserved.
doi:10.1016/j.supflu.2006.11.002

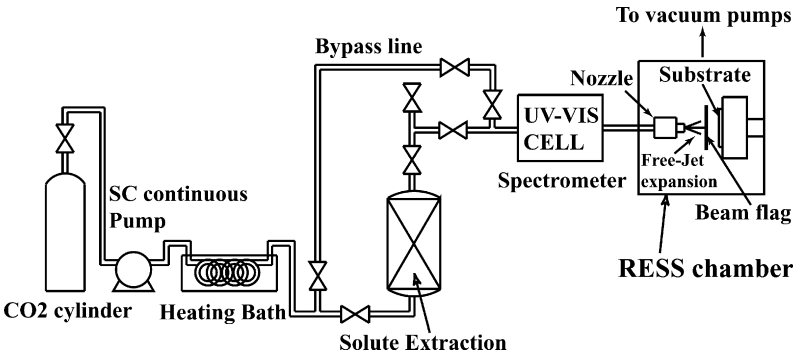

Fig. 1. RESS apparatus.

chamber where a 100 μm nozzle, beam flag and substrate are situated within a small vacuum chamber. The temperatures of the extraction vessel, the heating bath, the cell, the nozzle and the substrate are accurately controlled and monitored. The pure solvent is continuously pumped to the desired pressure and pre-heated to extraction temperature by circulating through the heated bath. The supercritical fluid is then passed through the extraction unit, which is a stainless steel vessel (9.5 cm^3 volume) packed with glass beads, where the solute is previously loaded as a powder. Subsequently the supercritical mixture flows through the spectroscopic cell where spectra of the solution are taken at regular intervals for determination of $Fe(acac)_3$ concentrations. Finally the supercritical solution is expanded from either a 100 μm orifice (aperture) nozzle source or a capillary nozzle source into the expansion chamber.

The fabrication of the 100 μm orifice and capillary nozzles has been described by Khalil [11,12]. The expansion properties for both of these RESS sources have been previously analyzed and described [11,12] theoretically by an axi-symmetric time-dependent numerical computation as well as experimentally with a shadowgraph method that captures the shock structure. The pressure in the expansion chamber, which can be reduced to 5×10^{-6} bar, is monitored with a MKS Baratron pressure transducer. The chamber is also equipped with a gas inlet for film growth in inert or oxidizing atmospheres. The doped-silicon substrate is placed on a substrate holder, which is connected to a micrometer translator to allow positioning of the plate to within 25 μm. The substrate is resistively heated and its temperature is monitored with a thermocouple placed between the substrate and the holder. Temperatures in excess of 200 °C can be easily maintained during film growth. When not heated, the substrate is cooled by the CO_2 jet to about −20 °C during film growth, which we refer to as a cold substrate condition below. A by-pass line allows pure solvent to purge the system and to establish steady state flow conditions. The experimental apparatus allows control of all the process variables: pre-expansion temperature, pressure, and composition of the initial solution, temperature of the substrate, position of the substrate with respect to the nozzle, and the expansion chamber pressure.

The UV–vis high-pressure, variable-volume, fiber-optic view cell used for the solubility measurement of $Fe(acac)_3$ in SC-CO_2 has been described in detail elsewhere [13]. The cell has been tested to 180 bar and 80 °C, is equipped with a stirrer, has a volume of 1.2 cm^3, and contains five quartz windows perpendicular to each other for both absorbance and light scattering measurements. Absorbance spectra are obtained with an Ocean Optics DH-2000 light source and HR2000 fiber optic spectrometer. Each fiber optic cable is connected to a collimating lens, which screws onto a cap that seals on the windows to obtain a fixed and well-aligned beam path. Experiments were typically performed with pressure and temperature control to a precision of ±0.5 bar and ±0.4 °C, respectively. The cell is used for both in-line concentration measurements and for equilibrium solubility measurements. In the latter case the cell is isolated from the pump and the expansion chamber.

The solubility is determined by a method developed by Ngo et al. [14] based on monitoring the change in intensity of $Fe(acac)_3$ UV–vis absorption peaks at 431 nm and 272 nm as a function of CO_2 density. Following Ngo, a known amount of solute is placed in a cell and the absorbance at 431 nm is measured as a function of CO_2 pressure, gradually increased from subcritical to supercritical pressures at constant temperature. The dissolution of $Fe(acac)_3$ in SC-CO_2 is detected as an increase in the absorbance. At each increased pressure value the absorbance is monitored as a function of time to be certain that saturation is achieved. Once all the solute in the cell is dissolved, an abrupt change in the slope of the absorbance versus pressure curve is observed and the absorbance becomes constant. The pressure at saturation is determined from the intersection of the constant absorption line and the line obtained by extrapolating the last data points before the absorbance plateau. The solubility can then be calculated by knowing the mass of the compound placed in the cell, the density of CO_2 at saturation, and the cell volume.

We also compared these absorption results with the commonly used cloud point method. This method is based on light scattering from the solute particles that precipitate out when the solution becomes supersaturated. In the experimental setup for cloud point measurement, the light source fiber optic is replaced with a Newport Research Corporation HeNe laser. The scattered light is detected with a CCD camera placed 90° respect to the laser beam interfaced with a TV monitor for qualitative observations. Solubility data are obtained fixing the temperature and varying the pressure until the cloud point is observed. While the two methods generally agreed to within 2%, we found that visually monitoring the light scattering was less repro-

ducible than monitoring a change in absorbance with the UV–vis spectrometer.

In this continuous-flow RESS apparatus the UV–vis cell is very important as a monitor of the in-line concentration prior to the rapid expansion because, due to mass transfer limitations, equilibrium is not reached in the extractor during continuous-flow operation. An important aspect of the spectroscopic measurements with our apparatus is the integrated data acquisition system that allows for real-time recording of temperature, pressure, spectra and concentration. Time-dependent profiles permitted us to know when equilibrium or steady state conditions were reached in either our solubility measurements or during the continuous RESS operation. We are able to maintain steady state source conditions for periods up to an hour during film growth, but typically for these studies we have grown films for only 10 min.

3. Results and discussion

3.1. Solubility measurements

In order to achieve better accuracy using the Ngo method described above, the absorption solubility experiments were performed after connecting a known larger volume (9.5 cm^3) to the UV–vis cell. The $Fe(acac)_3$ was weighed, in the milligram range, and added as a powder. In Fig. 2, our solubility data at 40 °C is compared to published solubility values obtained with a different method by Roggeman et al. [15]. We conducted our measurements at pressures compatible with our RESS film growth conditions, while most of Roggeman's data was concentrated at slightly higher pressures. The agreement between the two sets of data is satisfactory. We estimate that our solubility data are accurate within 4%.

Also shown in Fig. 2 is the solubility predicted by the Peng–Robinson equation of state (PR EOS), which is frequently used to predict phase behavior of solutes in supercritical solutions [4]. For the $Fe(acac)_3$, we followed Roggeman et al. [10] and took the critical values to be $P_c = 19.56$ bar, and $T_c = 526.8$ °C. The PR EOS has one interaction parameter, k_{12}, which we obtained by fitting experimental solubility data to the equation. In this manner we found $k_{12} = 0.152$. The other parameters in the equation are calculated from published thermodynamic data [16]. For the range of source conditions used in this investigation, the PR calculation and experimental data show that the solubility increases with increasing pressure and decreasing temperature. However, calculated solubility isotherms predict a cross-over pressure near 150 bar above which solubility increases with increasing temperature.

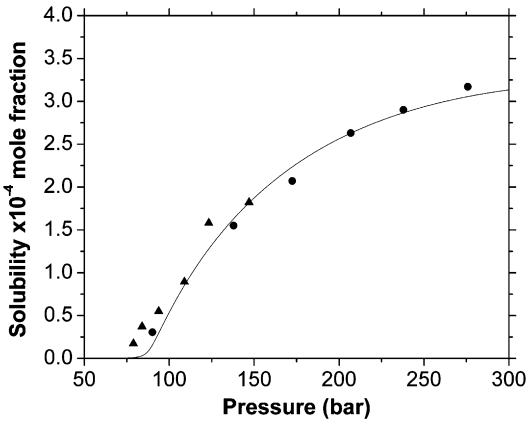

Fig. 2. Solubility of $Fe(acac)_3$ in SC-CO_2 at 40 °C.

From these equilibrium solubility data using our absorption method we were also able to extract the appropriate extinction coefficient of $Fe(acac)_3$ at different pressures. This data is important because it permits us to use the UV–vis cell for on-line monitoring of the dilute unsaturated SCF composition just prior to the RESS expansion. The extinction coefficient is found to be independent of temperature and pressure in our range of measurements. Calculated values of the extinction coefficient are $\varepsilon_\lambda = 2375$ l/(mol cm) at 431 nm and $\varepsilon_\lambda = 15{,}500$ l/(mol cm) at 272 nm. The extinction coefficient at 272 nm is used to determine the solubility in the lower pressure range given its high value.

3.2. Modeling of the RESS expansion and solute clustering

An advantage of the RESS process is that particle morphology and composition can be controlled by adjusting various process parameters. We have focused our initial studies on surveying the effects of SCF composition, substrate temperature, growth time, jet phase (liquid or vapor), nozzle geometry, nozzle to substrate distance, and expansion chamber pressure and composition. Although several parameters were varied, typical RESS expansion conditions for a vapor jet are stagnation pressure $P_o = 140$ bar, stagnation and extraction temperature $T_o = 70$ °C, nozzle-substrate distance $L = 1$ cm, hot substrate temperature $T_s = 200$ °C, and $Fe(acac)_3$ concentration in the stagnation chamber prior to the RESS expansion $X_o = 5 \times 10^{-6}$ mole fraction.

A difficult part of modeling the RESS process is to understand the clustering kinetics and fluid mechanics in the supersonic free-jet expansion [4,17–19]. We have completed axi-symmetric numerical computations for the free-jet expansion of supercritical CO_2 and compared them with measurements of the shock wave structure, and pressure and temperature measurements at a plate or substrate [11,12]. An example of the flow field and measured shock structure is shown in Fig. 3 [11,12,20]. To model the thermodynamics and clustering kinetics for our RESS expansion, an equivalent one dimensional nozzle shape was extracted from these more rigorous calculations, using stream tubes axi-symmetric to the jet centerline, so that we could apply a quasi-one dimensional (QOD) analysis [11,17–19]. This approximation can provide reasonable estimates of properties along the centerline of the jet expansion. It also reduces substantially the calculation time for the expansion and permits us to include more detailed clustering kinetic models. Given the large uncertainty of these kinetic models the QOD approximation seems sufficient to guide our experiments at this stage.

The expansion is conveniently visualized on a T–S diagram, as shown in Fig. 4, because it is an adiabatic expansion and closely approximates an isentropic expansion up to the shock-wave or until substantial irreversible CO_2 condensation occurs.

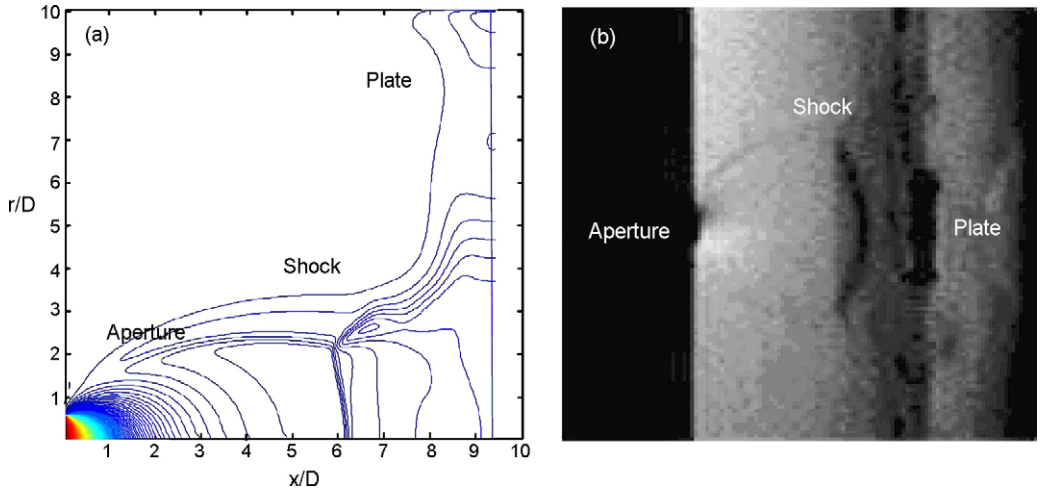

Fig. 3. CO_2 free-jet expansion ($T_o = 70\,^\circ C$, $P_o = 80$ bar) impacting a flat plate: (a) computed density profiles and (b) experimental shadowgraph measurement of the shockwave structure.

As indicated, by selecting the source conditions an expansion may occur on either the vapor or liquid side of the two-phase CO_2 region, so that clustering can occur in combination with condensation from a supersaturated vapor state (a vapor jet) or evaporation from the superheated liquid state (a liquid jet). Two such trajectories, typical of our RESS expansions, are indicated in Fig. 4. We have examined both experimentally and, as expected, found qualitatively different types of films. The details of our QOD modeling will be presented elsewhere, but Fig. 5 is an example of such a calculation for the centerline properties of a vapor jet as a function of distance measured in nozzle or orifice diameters (X/D). The properties are normalized by the stagnation conditions, except that X_o^* is the hypothetical concentration that would be saturated at P_o and T_o. The nozzle exit is at $X/D = 0$ and negative values are locations upstream of the exit in the subsonic flow while positive numbers are downstream of the exit in the supersonic flow. The temperature, pressure and equilibrium solubility profiles were calculated with the PR EOS. The solute concentrations are sufficiently low that the solute has negligible effect on the CO_2 expansion properties. The point in the expansion where, thermodynamically, the solute is predicted to precipitate depends on the actual initial source concentration. For example, if $X_o = 1 \times 10^{-6}$ mole fraction then $X_o/X_o^* = 0.5$ and Fig. 5 suggests the solute would become supersaturated and cross a cloud point near $X/D = -0.625$, upstream of the orifice exit or throat of the expansion. This point is before the point at which the CO_2 expansion pressure exceeds the saturation vapor pressure (P_{sat}) so that CO_2 could begin to condense ($X/D = 0.15$). However, the supersonic expansion is sufficiently rapid that the flow time scale for kinetic processes is of order microseconds and equilibrium is not achieved for many processes.

We have initiated our models of solute clustering by decoupling the kinetics from the solvent properties and ignoring the CO_2 solvent clustering. This is somewhat justified because we find, below, that the solute clustering should occur prior to solvent clustering. It remains a serious approximation because certainly mixed solute-solvent clusters are possible. We have previously analyzed the condensation of pure CO_2 solvent in the expansions and found that it can be substantial and have significant impact on the flow properties further downstream in the supersonic portion of the expansion [20]. A more complete model will need to be guided by mass spectrometer experiments

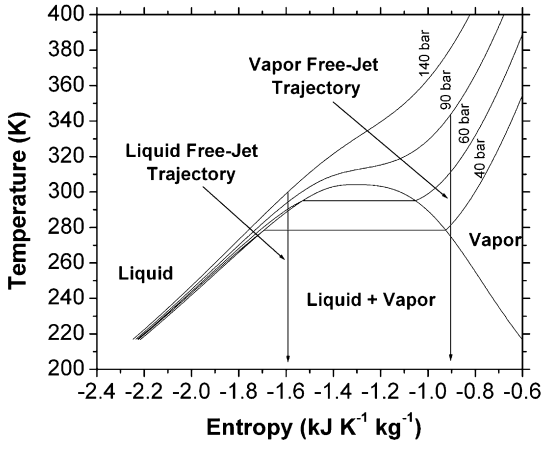

Fig. 4. Vapor and liquid jet adiabatic expansions visualized on a T–S diagram calculated with the software FLUIDCAL based on Wagner EOS for CO_2 [26].

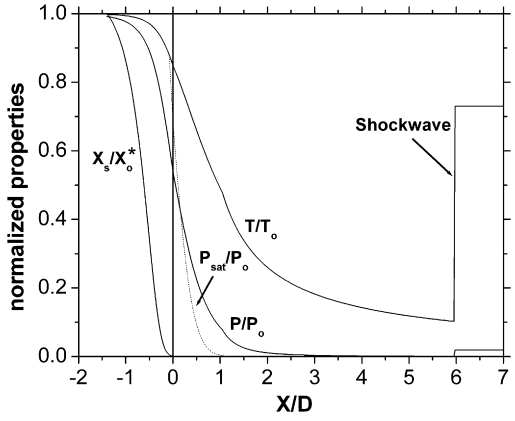

Fig. 5. Calculated centerline properties of a supersonic free-jet expansion. $P_o = 80$ bar, $T_o = 70\,^\circ C$, $X_o^* = 2.0 \times 10^{-6}$ mole fraction, $D = 100$ μm. Nozzle exit at $X/D = 0$.

which we are in the process of developing to probe the jets and assess what clusters are present.

Particle formation in supercritical fluids can be described using classical nucleation theory or using simplified collision kinetic models. Classical nucleation theory is not expected to be reliable for small clusters and certainly has difficulty assigning critical parameters, such as surface tension, to small nuclei. The classical theory is considered to be best for analyzing condensation of large drops with radii exceeding several nano-meters. In our expansions for example, the rigorous models of Debenedetti and co-workers [21] cannot be applied because the critical nuclei radius is estimated to be typically 0.3 nm or less, on the order of less than a single solute monomer, too small to render the classical model valid. Therefore we are pursuing kinetic models which have often been used to predict clustering in molecular beams [22]. The simplest clustering models consider only growth or evaporation by monomer addition or loss. Given the presence of high density CO_2 we have used a coupled diffusion-free molecular model for the growth of $Fe(acac)_3$ dimers and higher order clusters.

We describe cluster formation with a kinetic model based on a bimolecular collision between one molecule of $Fe(acac)_3$ and the cluster (or another $Fe(acac)_3$ molecule in case of dimer formation). We assume that the solute monomer molecules diffuse in supercritical CO_2 to within a mean free path of an existing cluster, or other monomer, and then undergo a free molecular collision with the cluster surface. We describe the collision with a one-step mechanism on the assumption that the $Fe(acac)_3$ molecule and clusters can dissipate the excess energy in their vibrational modes, but we add an adjustable sticking coefficient parameter to account for the probability of monomer attachment. The calculation is straightforward using simple kinetic expressions for bimolecular collision rates. This series rate process then gives the resulting rate for cluster growth as

$$R_i = \frac{n_1 \times n_{(i-1)}}{(1/4\pi D r_\lambda) + (1/\alpha v \pi r^2)} \quad (1)$$

where R_i is the number of clusters made of i monomers formed per unit volume per unit time, n_1 the number density of the solute monomer, $n_{(i-1)}$ the number density of clusters of size $i-1$, $D(T, P)$ the diffusion coefficient of the solute in CO_2, r_λ the radius of the cluster plus the mean free collision path, α the sticking coefficient, $v(T)$ the mean molecular thermal velocity and r is the radius of the cluster. At high densities the rate is diffusion controlled but as the expansion proceeds and the density falls the rate becomes controlled by the free molecular bimolecular collision rate. The net rate of growth for each cluster size includes four terms, production terms due to growth from a smaller cluster and evaporation from a larger cluster, and loss terms due to growth to a larger cluster and evaporation to a smaller cluster [22]. We find that, due to the low vapor pressure of $Fe(acac)_3$, the terms for monomer loss by evaporation are not important for our expansions. Additional details will be given elsewhere, but the set of coupled ordinary differential equations, one for net rate of cluster growth for each cluster size, is numerically integrated along the axis of the expansion to calculate the mass fraction of clusters along the jet. The calculation is started at the position where the solute becomes supersaturated so that thermodynamically the condensed phase is stable. The cluster formation equations are very stiff and a suitable ODE solver was found to be the Matlab ode15s for stiff equations.

As an example, Fig. 6(a) is a plot of the centerline cluster mass fraction versus distance assuming a unity sticking coefficient ($\alpha = 1$), which gives the maximum rate of cluster growth. This result indicates that most of the condensation occurs in less than one nozzle diameter, just upstream and before the throat. After the nozzle exit there is no further growth of the clusters, solute trimer clusters are the largest mass fraction but some pentamer clusters are possible. However, we do not find large nano-scale clusters even after adjusting the parameters over reasonable ranges of values. There are obviously several poorly known parameters in the model, including the diffusion coefficient (estimated with the Stokes–Einstein equation), the collision cross-sections, the cluster geometry (taken as spherical for our simplified model), and the sticking coefficient for monomer addition which is the most sensitive parameter. To illustrate how sensitive the model is to the sticking coefficient, Fig. 6(b) shows the results assuming $\alpha = 0.1$. The cluster yield drops from 96% to 62% with dimers becoming the dominant species. As we show below the range of particle size present in

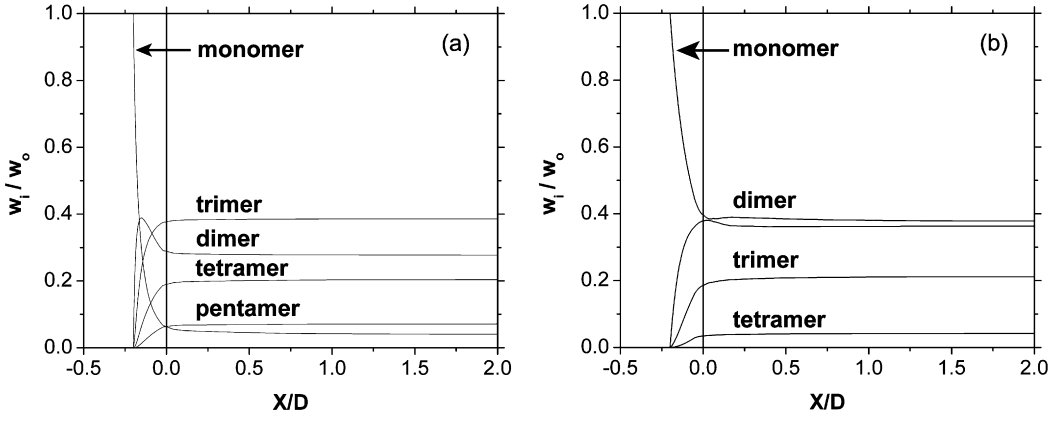

Fig. 6. $[Fe(acac)_3]_i$ cluster mass fraction, normalized by monomer initial mass fraction, vs. distance, normalized by nozzle diameter. $T_o = 70\,^\circ C$, $P_o = 140$ bar, $w_o = 5.6 \times 10^{-5}$, $D = 100$ μm: (a) sticking coefficient $\alpha = 1$ and (b) sticking coefficient $\alpha = 0.1$.

our thin films is much larger than the small molecular clusters predicted in our kinetic model. This result clearly suggests that the particles are growing on the substrate and not in the RESS expansion for the conditions of our experiments.

We are extending our calculations to include condensation of the solvent CO_2 and also mixed clusters, but we will require experimental measurements of the jet composition to begin to assess the value of such models, and to empirically adjust sensitive parameters. To obtain such data, we are interfacing our RESS expansion directly with a time-of-flight mass spectrometer so that we can compare cluster composition data with our clustering models, and better understand the composition of the fluid which strikes the substrate.

3.3. Characterization of the cluster films

Magnetic thin films are produced by rapidly expanding the supercritical solution of $Fe(acac)_3$ and CO_2 and directing the resulting supersonic jet onto both hot and cold silicon wafers. The substrate temperature can be increased above 200 °C such that thermal decomposition of the solute may occur at the Si surface with subsequent formation of iron oxide magnetic particles. Langlet et al. [3] has shown that at these temperatures he was able to form either γ-Fe_2O_3 or Fe_3O_4 depending on the decomposition temperature and on the percentage of oxygen present in the deposition chamber.

The deposited particle films were removed and analyzed with a FEI Quanta 600 Scanning Electron Microscope (SEM), including energy dispersive X-ray (EDX) which gives qualitative elemental analysis, and a Quantum Design MPMS-XL5AC superconducting quantum interference device (SQUID) based magnetometer. In the results presented below, for particle size we used the classification of Reverchon and Adami [9] to indicate that the particles belong to either the nano- or sub-micronic category depending on experimental conditions.

In Fig. 7, SEM images of a typical film from the supersonic free-jet expansion of a CO_2/$Fe(acac)_3$ mixture on a cold substrate ($T_s \sim -5$ °C) are shown. Fig. 7(a) shows the entire film region and it is found that the size of the center spot is characteristic of the size of the jet shock structure (~3 mm) indicated in Fig. 3. Fig. 7(b) is a closer view of the center of the expansion. This film is made of both nanoparticles and sub-micronic particles with a minimum size of 110 nm, maximum size of 700 nm, mean size of 260 nm and standard deviation of 110 nm. In general smaller nanoparticles are formed on a cold substrate when the expansion is into vacuum and the growth time is kept below 10 min. This could be an effect of the different shock wave structure between free-jet expansions into vacuum versus into one atmosphere. For example, expansion into low pressures leads to a weaker shock structure. The density then remains low and the velocity high so that both the flow time and density is less favorable for the growth of larger clusters. In contrast, when the flow passes through a strong shock, the density increases substantially and the flow velocity is reduced, both of which could favor additional cluster growth downstream of the shock. The effect of the growth time suggests that growth on the surface is also very important, since bigger particles are observed

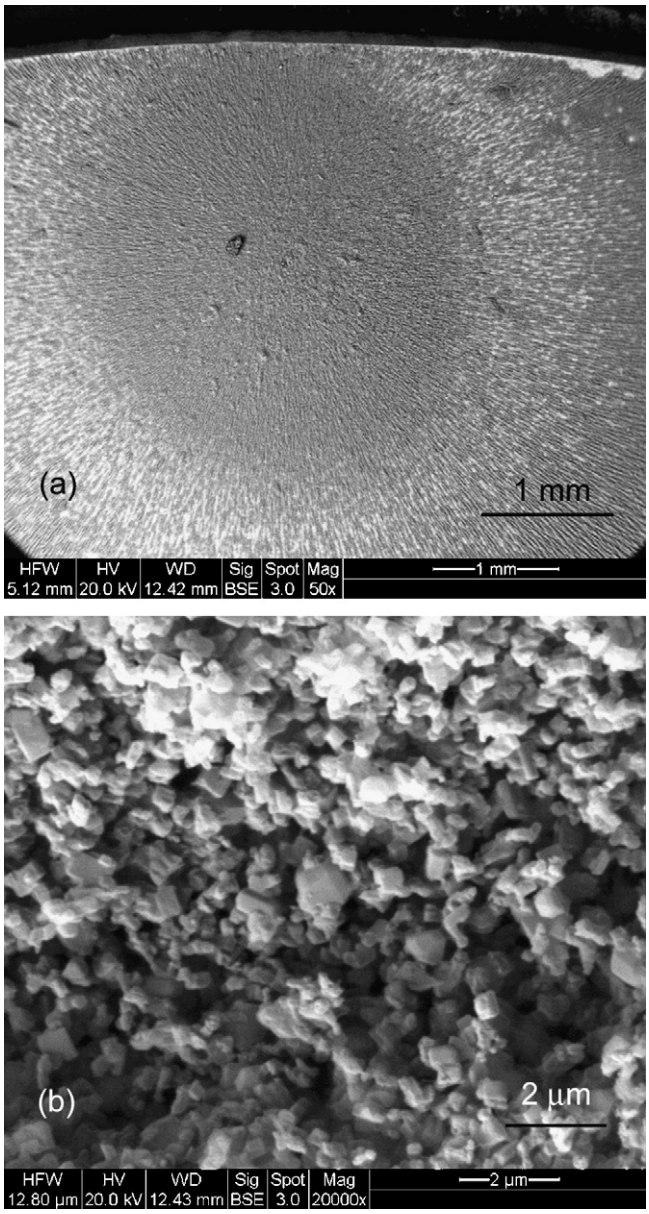

Fig. 7. Film deposited from a CO_2/$Fe(acac)_3$ mixture expanded from a 100 µm orifice nozzle on a cold substrate. $P_o = 140$ bar, $T_o = 70$ °C, nozzle-substrate distance = 10 mm, 1 atm N_2 background, $T_s = -5$ °C.

with longer growth times. In addition we find that decreasing the stagnation pressure leads to smaller particles, an indication that both kinetics and thermodynamics influence cluster growth in the RESS expansion. These experimental results and our simple kinetic models described above suggest that while the RESS jet may provide very small seed clusters, it is most likely that substantial growth to the larger nano- and sub-micronic scale particles is occurring at the surface itself.

A typical nanoparticle film on a hot substrate is shown in Fig. 8. In this particular case the free jet was directed against a cold substrate and subsequently heated to 200 °C once the deposition was completed. In this film the particles are much smaller than the cold samples, since they have a minimum size of 13 nm and a maximum size of 120 nm. In particular, nanopar-

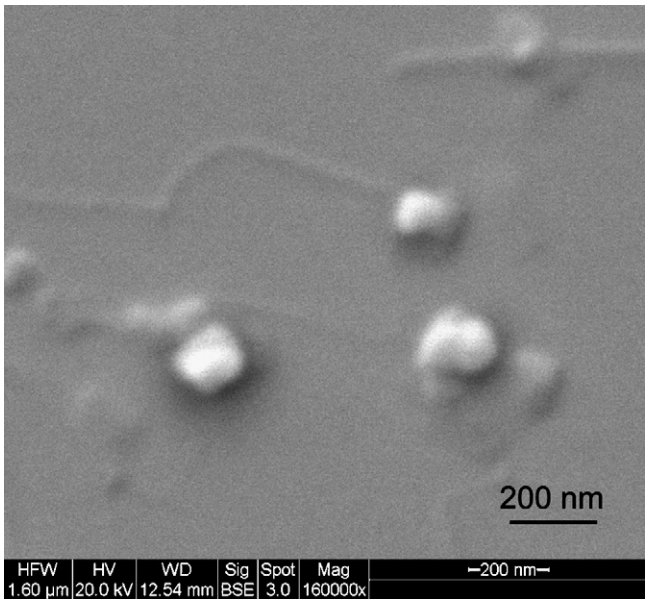

Fig. 8. Film deposited from a CO_2/Fe(acac)$_3$ mixture expanded from a 100 μm orifice nozzle on a hot substrate. $P_o = 140$ bar, $T_o = 70\,^{\circ}C$, nozzle-substrate distance = 10 mm, 1 atm N_2 background, $T_s = 200\,^{\circ}C$.

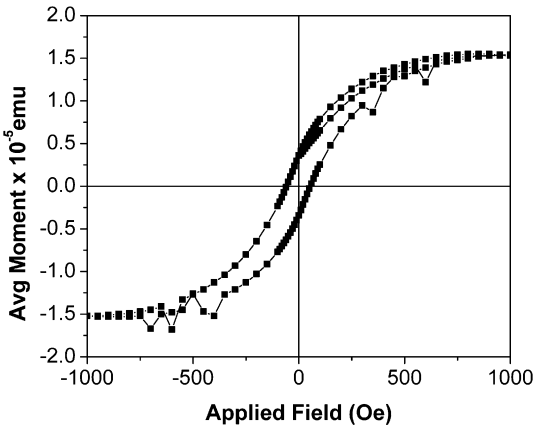

Fig. 9. Magnetization vs. applied field at 2 K; film deposited on a hot substrate. $P_o = 140$ bar, $T_o = 70\,^{\circ}C$, nozzle-substrate distance = 10 mm, 1 atm N_2 background, $T_s = 200\,^{\circ}C$.

ticles shown in Fig. 8 have a mean size of 70 nm and a standard deviation of 25 nm. Although an SEM image is not reported here given the low contrast in the picture, nanoparticles with an average size of 30 nm have also been synthesized by free jet deposition directly onto a hot substrate. The formation of smaller nanoparticles on the hot substrate could be caused by lower sticking upon impact on a hot surface or increased evaporation from the hot surface before significant surface cluster growth. The morphology of the particles is quite uniform if the growth time is kept under 10 min or if the expansion is conducted in vacuum.

There are many RESS variables that clearly require further study, both experimentally and theoretically, and for which we have only qualitatively surveyed to date. For example, when the nozzle-to-substrate distance is reduced below 5 mm we find poor uniformity of the films with an apparent loss of material in the center of the film, along the jet axis. This may be due to the impact of the jet and subsequent removal of film material. Solute concentration also has a role in determining particle size and morphology and we found that more uniform and smaller particles were obtained by lowering Fe(acac)$_3$ concentration from 9×10^{-6} to 3×10^{-6} mole fraction. We have also explored a few films deposited under a different stagnation temperature ($T_o = 50\,^{\circ}C$) such that clustering would occur in a liquid jet. In this regime we observed a decrease in particle size but the films obtained from the liquid phase RESS jet were less uniform than those formed in the vapor phase jet.

Magnetization measurements on several of these cluster films were performed with a SQUID-based magnetometer on samples formed on both cold and hot substrates, in vacuum and at 1 atm N_2. Magnetic moment versus applied field measurements were performed at 2, 5, and 300 K, applying a maximum field of 4 T, in order to assess both the paramagnetic and ferromagnetic contributions. Fig. 9 shows a typical hysteresis loop for the iron oxide particles formed on a hot substrate. This sample has a coercivity (H_c) of 55 Oe, a saturation magnetization of 1.5×10^{-5} emu and a remanent magnetization of 3.6×10^{-6} emu. The coercivity is an interesting characteristic of cluster type films because it is known to be sensitive to particle size or film thickness [23]. Typically as particle size is reduced the coercivity increases from the continuum bulk film, passes through a maximum near the regime where the magnetic behavior changes from multi-domain to single-domain and then decreases to zero when the smallest particles become superparamagnetic. Our measured bulk values of H_c for α-Fe_2O_3 and Fe_3O_4 are typically of order 1300 Oe and 150 Oe respectively and reported values for γ-Fe_2O_3 are of the order 300 Oe [24]. While our results for H_c would be consistent with single domain iron-oxide magnetic particles of order 50 nm such a result is not conclusive and requires a better knowledge of the structure and composition of the magnetic particles. We have done a limited amount of Mössbauer spectroscopy to identify the iron oxide phase. This is a difficult measurement to make given the small amount of material on the samples. We are still uncertain on which iron oxide phase is present on the substrate although, for one sample, we fitted the data with a sextet whose parameters agree with α-Fe_2O_3 [25].

Despite the fact that the starting material is paramagnetic and the substrate is diamagnetic we find that the films grown on cold substrates also show similar magnetic order; this surprising result is shown in Fig. 10. This sample has a coercivity of 58 Oe, a saturation magnetization of 1.4×10^{-5} emu and a remanent magnetization of 2.8×10^{-6} emu, data which would again suggest the magnetic particles in the films are of a size of order 50 nm. These magnetic signatures are very typical and have been reproduced consistently for the hot and cold samples, with SQUID measurements at both 2 K and 300 K. The magnetically ordered signal is comparable for the hot and cold samples but the cold samples also have a paramagnetic contribution at 2 K. The magnetically ordered signal on the cold substrates suggests that paramagnetic Fe(acac)$_3$ decomposed to a magnetically ordered compound without any subsequent heat treatment. A Mössbauer analysis of the paramagnetic phase for one of the cold samples also suggests the presence of one of the intermediate products expected in the thermal decomposition of Fe(acac)$_3$

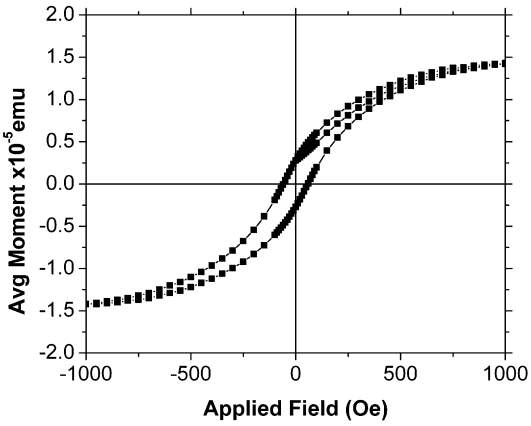

Fig. 10. Magnetization vs. applied field at 300 K; film deposited on a cold substrate. P_o = 140 bar, T_o = 70 °C, nozzle-substrate distance = 10 mm, 0.013 bar N_2 background, T_s = −5 °C.

to Fe_3O_4 [25]. Over the limited range of conditions in our RESS experiments, we have not observed substantial changes in the coercivities we have measured and they are all consistent with the formation of magnetic nanoparticles.

The mechanism for the decomposition of $Fe(acac)_3$ in our RESS experiment on a cold substrate with no heat treatment is difficult to explain and is the most surprising result of our experiments to date. In an expansion into vacuum without shock waves the heavy $Fe(acac)_3$ monomers and clusters can be accelerated by the CO_2 carrier gas [18]. For the monomer unit we calculate that translational energies in excess of 30 kJ/mol can be obtained before they impact the substrate surface, and this energy can be greater for dimers, trimers, etc. However, we also find magnetic order on cold substrates when the RESS expansion occurs at ambient conditions and where the shock wave would in fact slow down the heavy particles to values of order 1 kJ/mol. Further, since the bond energy of the Fe–O bond in $Fe(acac)_3$, the weakest in the compound, has a value of about 151 kJ/mol [11], we do not expect that the translational impact energy is sufficient in either case. Therefore the mechanism for the decomposition remains an interesting dilemma which we need to investigate further. We are in the process of setting up batch experiments to assess whether the decomposition can occur in bulk supercritical solution in the absence of a RESS expansion.

4. Conclusion

We have developed and tested a continuous-flow RESS apparatus to produce magnetic nano- and sub-micronic particle films using the supercritical solution $Fe(acac)_3$ in CO_2. SQUID and SEM magnetic and structural data for these thin particle films show that the films are magnetically ordered for both cold and hot substrates, and the particle size ranges from 13 nm to 700 nm depending on the experimental conditions. A simplified cluster growth model for the RESS expansion suggests that most of the particle growth occurs on the surface and not in the expansion. Contrary to expectation, we are able to form magnetic particle films without the need to grow the films on high temperature substrates or in an oxidizing atmosphere.

Acknowledgments

This work was partially supported by the National Science Foundation grant CHE-0136195. We gratefully acknowledge Dr. James O'Brien of Quantum Design for the magnetic measurements and Fred Parker from UCSD CMRR for the Mössbauer measurements.

References

[1] P.S. Shah, S.H. Husain, K.P. Johnson, B.A. Korgel, Nanocrystal arrested precipitation in supercritical carbon dioxide, J. Phys. Chem. B 105 (2001) 9433.
[2] R.M. Cornell, U. Schwertmann, The Iron Oxides, Wiley–VCH, Weinheim, 2003.
[3] M. Langlet, M. Labeau, B. Bochu, J. Joubert, Preparation of thin films in the system γFe_2O_3–Fe_3O_4 for recording media by spray pyrolysis of organometallic solutions using an ultrasonic pump, IEEE Trans. Magn. 3 (1986) 151.
[4] Y. Arai, T. Sako, Y. Takebayashi, Supercritical Fluids: Molecular Interactions, Physical Properties, and New Applications, Springer, New York, 2001.
[5] R. Petersen, D. Matson, R. Smith, Rapid precipitation of low vapor pressure solids from supercritical fluids solutions: the formation of thin films and powders, J. Am. Chem. Soc. 108 (1986) 2102.
[6] J. Brand, D.R. Miller, Deposition of thin alumina films from supercritical water jets, chemical perspectives of microelectronics devices, Mater. Res. Soc. 131 (1989) 617.
[7] M. Türk, P. Hils, B. Helfgen, K. Schaber, H.-J. Martin, M.A. Wahl, Micronization of pharmaceutical substances by the rapid expansion of supercritical solutions (RESS): a promising method to improve bioavailability of poorly soluble pharmaceutical agents, J. Supercrit. Fluids 22 (2002) 75.
[8] N. Levit, D. Pestov, G. Tepper, High surface area polymer coatings for SAW-based chemical sensor applications, Sens. Actuators B 82 (2002) 241.
[9] E. Reverchon, R. Adami, Nanomaterials and supercritical fluids, J. Supercrit. Fluids 37 (2006) 1.
[10] J.A. Darr, M. Poliakoff, New directions in inorganic and metal-organic coordination chemistry in supercritical fluids, Chem. Rev. 99 (1999) 495.
[11] I. Khalil, D.R. Miller, The structure of supercritical fluid free-jet expansions, AIChE J. 50 (2004) 2697.
[12] I. Khalil, D.R. Miller, The free-jet expansion of supercritical CO_2 from a capillary source, in: M. Capitelli (Ed.), Proceedings of the 24th International Symposium on Rarefied Gas Dynamics, Am. Inst. Phys. Conf. Proc. 762 (2005) 343.
[13] S. De Dea, Metal chelate processing in supercritical carbon dioxide, MS thesis, University of California, San Diego, 2004.
[14] T. Ngo, D. Bush, C.A. Eckert, Spectroscopic measurement of solid solubility in supercritical fluids, Thermodynamics 47 (2001) 2566.
[15] E.R. Roggeman, A.M. Scurto, J.F. Brennecke, Spectroscopy, solubility and modeling of cosolvent effects on metal chelate complexes in supercritical carbon dioxide solutions, Ind. Eng. Chem. Res. 40 (2001) 980.
[16] M.A.V. Ribeiro da Silva, M.J.S. Monte, Vapor pressures and standard molar enthalpies of sublimation of two crystalline iron(III) β-diketonates. The mean molar (Fe–O) bond-dissociation enthalpies, J. Chem. Thermodyn. 28 (1996) 413.
[17] M. Weber, M. Thies, in: Y. Sun (Ed.), Supercritical Fluid Technology in Material Science and Engineering, Marcel Dekker, Inc, New York, 2002, p. 387.
[18] D.R. Miller, Free jet sources, in: G. Scoles (Ed.), Atomic and Molecular Beam Methods, vol. 1, Oxford University Press, New York, 1998, p. 14.
[19] E. Reverchon, P.J. Pallado, Hydrodynamic modeling of the RESS process, J. Supercrit. Fluids 9 (1996) 216.
[20] I. Khalil, Free-jet expansion of supercritical CO_2, PhD thesis, University of California, San Diego, 2003.

[21] J.W. Tom, P.G. Debenedetti, Particle formation with supercritical fluids—a review, J. Aerosol Sci. 22 (1991) 555.
[22] J.T. McDaniels, R.E. Continetti, D.R. Miller, The effect of nozzle geometry on cluster formation in molecular beam sources, in: Ketsdever, Muntz (Eds.), Proceedings of the 23rd International Symposium on Rarefied Gas Dynamics, Am. Inst. Phys. Conf. Proc. 663 (2003) 670.
[23] B.D. Cullity, Introduction to Magnetic Materials, Addison-Wesley Pub. Co., Reading, MA, 1972, p. 386.
[24] L. Zhang, G.C. Papaefthymiou, J.Y. Ying, Size quantization and interfacial effects on a novel γ-Fe_2O_3/SiO_2 magnetic nanocomposite via sol-gel matrix mediated synthesis, J. Appl. Phys. 81 (1997) 6892.
[25] N.B. Morozova, V.N. Mit'kin, I.K. Igumenov, V.A. Varnek, O.G. Potapova, The thermal decomposition of iron(III) tris(acetylacetonate) in the condensed state, Russian J. Inorg. Chem. 33 (1988) 1459.
[26] R. Span, W. Wagner, A new equation of state for carbon dioxide covering the fluid region from the triple-pint temperature to 1100 K at pressures up to 800 MPa, J. Phys. Chem. Ref. Data 25 (1996) 1509.